Available online at www.sciencedirect.com

ScienceDirect

Energy Procedia 114 (2017) 3113 – 3131

Energy Procedia

13th International Conference on Greenhouse Gas Control Technologies, GHGT-13, 14-18 November 2016, Lausanne, Switzerland

Vertical equilibrium flow models with fully coupled geomechanics for CO_2 storage modeling, using precomputed mechanical response functions

O.A. Andersen[a,b,*], H.M. Nilsen[a], S.E. Gasda[c]

[a] *Sintef ICT, Dept. of Applied Mathematics, PO Box 124 Blindern, N-0314 Oslo, Norway*
[b] *Department of Mathetmatics, University of Bergen, Norway*
[c] *Uni Research CIPR, PO Box 7810, N-5020 Bergen, Norway*

Abstract

Vertical equilibrium (VE) models have proved to be attractive for simulation of CO_2 storage scenarios. Their primary advantage is a substantial reduction in computational requirements compared to standard 3D simulation tools. In this work, we aim to include the effects of geomechanics on aquifer flow while preserving computational efficiency. When fluids are injected into a geological formation, changes in pore pressure leads to rock deformation, which influence the flow properties of the formation. To fully model this effect, a two way coupling between flow and mechanics equations is generally necessary, including the full under- and overburden. This leads to a computationally expensive system, thus reducing the computational advantage of using VE models. Within a linear poroelastic framework, the full effect of deformation on flow is captured through changes in volumetric strain, which can be precomputed for a given pressure basis at grid generation time and used directly in the flow equations during simulation. This allow us to model the full effect of geomechanics on aquifer flow while eliminating the need for solving the mechanics equations at simulation time. We demonstrate the approach on 2D and 3D examples, and compare with results obtained from a standard VE flow models and a model that includes the full poroelastic set of equations. Compared to the latter, we observe a significant computational benefit using our proposed approach. On the other hand, the impact of geomechanics appears to be primarily captured by a well-chosen rock compressibility coefficient, suggesting that a fully coupled model might not be required in many practical cases.

Peer-review under responsibility of the organizing committee of GHGT-13.

Keywords: vertical equilibrium; linear poroelasticity; poromechanics; CCS

* Corresponding author.
E-mail address: odd.andersen@sintef.no

Peer-review under responsibility of the organizing committee of GHGT-13.
doi:10.1016/j.egypro.2017.03.1440

1. Introduction

The storage of CO_2 in the subsurface is a key component of carbon capture and storage (CCS) strategies, which have been widely proposed as a strategy to combat climate change. In order for CCS to contribute meaningfully to global mitigation goals, very large amounts of CO_2 needs to be geologically stored, calling for large-scale operations and geological sites that can store hundreds of megatonnes of CO_2 for thousands of years [1].

Like any fluid injection or extraction operation in the subsurface, the storage of large amounts of CO_2 within a geological formation will lead to significant changes in the fluid pressure field. Changes in the underground balance between pressure and mechanical forces will lead to some degree of deformation in the rock matrix, which again affects important flow parameters, in particular rock porosity and permeability. To properly account for these effects, the modeling of fluid flow in a storage aquifer will need to be coupled with a geomechanical model that includes not only the aquifer itself but also the surrounding rock matrix. In the context of CO_2 storage, this has been done in e.g. [2,3] and [4]. The full coupling between flow and geomechanics is significantly more computationally demanding than the solution of the flow equations in isolation. Operator splitting strategies have been developed to allow such coupled problems to be solved more efficiently [5,6]. This approach makes it possible to use separate solvers for the flow and mechanics part of the problem, allowing re-use of existing, highly sophisticated simulation tools. On the other hand, the computational requirements remain high, and access to both types of solvers is required at simulation time.

Compared with conventional reservoir simulation, the modeling of CO_2 storage and long-term migration must take very large spatial and temporal scales into account, and involves fluid phenomena that are numerically difficult to capture using industry-standard 3D flow simulators [7,8]. Consequently, the last decade has seen an increased focus in the research community on simplified models, in particular models derived from the assumption of vertical equilibrium (VE). Such models were initially developed for reservoir simulation when computing resources were scarce [9–11], and have more recently been reintroduced in the context of CO_2 storage [12]. VE models are advantageous in that they reduce the dimensionality of the problem, leading to a significant reduction in computational requirements. Moreover, they provide "infinite vertical resolution", and therefore allow accurate modeling of thin gas tongues below a confining caprock. Past studies indicate that results from VE models compare well with those obtained from conventional 3D simulation [13,14]. VE models for simulating CO_2 storage have been developed to include effects such as capillarity [15], dissolution [16], compressibility [17], caprock rugosity [18] and thermal effects [19]. A simplified geomechanical model for use in a VE context was recently proposed in [20].

The low computational cost of VE models permits their use in workflows that require a large number of independent simulations, such as in the optimization of injection rates [21] or model calibration based on measured historical data [22]. In order for such use cases to remain possible, the inclusion of geomechanical impacts in the VE framework must be done in a way that does not change computational requirements with orders of magnitude. In [20], a simplified mechanical model for the aquifer is proposed, but the method still requires a full mechanical model for the surrounding rock matrix and the access to a dedicated mechanical solver at simulation time.

In the present work, we propose a method that allow us to include the full impact of geomechanics on flow to any desired degree of approximation, while dispensing with the need to couple with a mechanics solver during simulation. We achieve this by precomputing mechanical responses for a set of pressure basis functions and storing these in approximate form with the simulation grid. These responses are then used by the flow simulator in a manner similar to the common use of pore volume compressibility coefficients in conventional reservoir simulators. Our work extends on previous results in [23] by including two-phase flow, heterogeneous flow properties and strain-dependent permeability, using a vertical equilibrium approach for the flow equation. Details on the approach is described in Section 2 and Section 3. We provided some results using a 2D and 3D case in Section 4 and discuss the observed impact and related issues in Section 5.

2. Mathematical model

2.1. The physical system

We considered CO_2 injection into an aquifer surrounded by an over- and underburden, as illustrated in Figure 1. The permeability of the aquifer is sufficiently high to permit practical storage of CO_2, whereas the surrounding rock is considered impermeable and only included for its mechanical impact on the system. While the figure shows a flat aquifer truncated at its lateral boundaries, our model may also include more general geometries and lap-outs or otherwise vanishing aquifer boundaries, but it is assumed that the aquifer remains thin compared to its lateral extent. In what follows, we will denote the aquifer domain by Ω_A and the surrounding rock matrix by Ω_S. Fluid flow will thus only be considered in Ω_A, whereas mechanical deformation occurs throughout $\Omega = \Omega_A \cup \Omega_S$.

In this model, the top surface is free to move, i.e. the mechanical boundary condition is that of fixed (zero) stress. The mechanical conditions on other boundaries may be freely chosen; our examples in Section 4 consider lateral roller conditions (as indicated on figure) or clamped conditions.

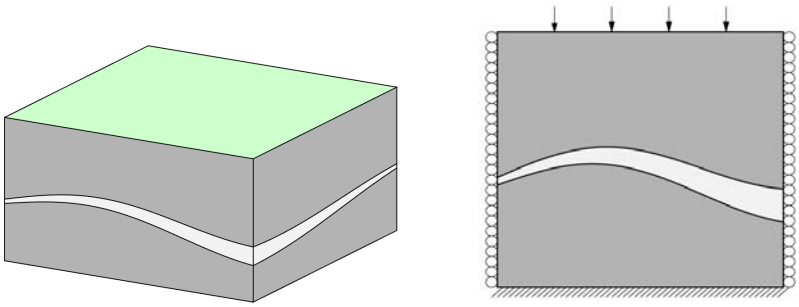

Fig. 1. *Left:* The conceptual model. The aquifer is illustrated as a light band within a darker matrix of surrounding rock that extends up to the ground level (green surface). Fluid flow only takes place in the aquifer, whereas mechanical deformations are computed for the full model. *Right:* Cross-section view of the model, with mechanical boundary conditions indicated. Lateral boundaries can be of any type ('roller' type indicated on figure).

2.2. The poroelastic model

Since CO_2 storage operations typically do not involve significant compaction, we here assume that principal stresses remain within the yield surface of the rock, with elastic material behavior. We describe the coupled system involving rock deformation and fluid pressure within the theory of linear poroelasticity [24]. The system consists of a set of force balance equations for mechanical stresses and a conservation equation for fluid flow, coupled by terms that involve fluid pressure and volumetric strain.

The force balance equations describes a poromechanical system in static equilibrium the a spatial domain Ω with boundary $\partial\Omega$. Rotational equilibrium implies symmetry of the total stress tensor $\boldsymbol{\sigma}$, which will be automatically satisfied by our constitutive model, whereas translational equilibrium requires that body forces $\mathbf{f}$ are counterbalanced by the divergence of stress:

$$\nabla \cdot \boldsymbol{\sigma} + \mathbf{f} = 0 \tag{1}$$

With the convention that tensile stresses are *positive*, total stress equals the difference between *effective stress* $\boldsymbol{\sigma}'$ and pore pressure scaled by the *Biot-Willis coefficient* α:

$$\boldsymbol{\sigma} = \boldsymbol{\sigma}' - \alpha p \mathbf{I} \tag{2}$$

Effective stress and elastic stain $\boldsymbol{\epsilon}$ are linked using Hooke's law, where $\mathbf{C}$ is a fourth-order elasticity tensor:

$$\boldsymbol{\sigma}' = \mathbf{C}\boldsymbol{\epsilon} \tag{3}$$

and the elastic strain tensor is defined in terms of 3D displacements **u** as:

$$\boldsymbol{\epsilon} = \frac{1}{2}\left(\nabla\mathbf{u} + (\nabla\mathbf{u})^T\right) \tag{4}$$

For an isotropic material, **C** can be entirely described by two elastic moduli, e.g. bulk K and shear G moduli, which are allowed to be spatially heterogeneous. In particular, there may be a contrast in elastic properties between the aquifer and the surrounding rock. Considering the body force to consist of gravity, i.e. $\mathbf{f} = -\rho_b\mathbf{g}$ with ρ_b being bulk density and **g** gravitational acceleration, and combining (1)-(4), we obtain the following expression for mechanical equilibrium that includes fluid pressure:

$$\nabla\cdot(\mathbf{C}\boldsymbol{\epsilon}) - \nabla(\alpha p) = \rho_b\mathbf{g} \tag{5}$$

Boundary conditions are defined independently for each spatial component, and subdivide $\partial\Omega$ into parts with imposed stress and parts with imposed displacements.

In a one-phase fluid system, the flow equation can be written on the form:

$$\left(\frac{1}{K}(1-\alpha)(\alpha-\phi) + \frac{1}{K_f}\phi\right)\frac{\partial p}{\partial t} + \alpha\frac{\partial\epsilon}{\partial t} + \nabla\cdot\mathbf{q} = \psi \tag{6}$$

Here, K and K_f represent the rock and fluid bulk moduli, ϕ the rock porosity, $\epsilon = \mathrm{tr}(\boldsymbol{\epsilon})$ volumetric strain, **q** volumetric flux and ψ a source term. The accumulation term consists of one part depending on pressure and another depending on volumetric strain. The pressure dependent term can be subdivided into separate terms for grain and fluid compressibility. the volumetric flux **q** can be linked to fluid pressure through Darcy's law:

$$\mathbf{q} = -\frac{k}{\mu}(\nabla p - \rho_f\mathbf{g}z) \tag{7}$$

where k represents the permeability of the medium, μ fluid viscosity and ρ_f fluid density. As previously stated, fluid flow occurs in the aquifer only, i.e. our flow domain is limited to Ω_A. Boundary conditions consists of a subdivision of $\partial\Omega_A$ into regions of imposed flux and regions of imposed pressure, where the top and bottom surface of Ω_A are assumed to be of the first type, with zero flux (impermeable caprock).

Together, (5) and (6) describe the poroelastic system. The coupling between mechanics and flow occurs in the form of a pressure term $\nabla(\alpha p)$ in the flow equation and a volumetric strain term $\alpha\epsilon$ in the flow equation.

2.3. Two-phase flow and vertical equilibrium (VE) formulation

We expand the basic poroelastic system by introducing two fluid phases representing CO_2 and resident brine. This means introducing phase saturations s_α and pressures p_α, and replacing (6) with separate flow equations for each phase, on the form:

$$\phi\frac{\partial s_\alpha}{\partial t} + s_\alpha\left[\left(\frac{\phi}{K_{f,\alpha}} + \frac{1}{K}(1-\alpha)(\alpha-\phi)\right)\frac{\partial p_\alpha}{\partial t} + \alpha\frac{\partial\epsilon}{\partial t}\right] + \nabla\cdot\mathbf{q}_\alpha = \psi_\alpha \tag{8}$$

$K_{f,a}$ now represents the inverse compressibility of phase α (CO_2 or brine), which might depend on pressure (i.e. we do not require linearity). ψ_α is a source term proper to phase α, whereas $\mathbf{q}_\alpha$ is the phase flux described by the multiphase extension to Darcy's equation:

$$\mathbf{q}_\alpha = -\lambda_\alpha k(\nabla p_\alpha - \rho_\alpha\mathbf{g}z) \tag{9}$$

For the coupling term $\nabla(\alpha p)$ with the mechanics equations, we here employ a simple weighted average of phase pressures:

$$p = \sum_\alpha s_\alpha p_\alpha \tag{10}$$

The vertical equilibrium formulation is obtained by assuming negligible vertical flow, which signifies that the vertical pressure profile is considered hydrostatic. Furthermore, phase segregation is assumed, so that CO_2 is present as a separate zone of local thickness h wedged between the confining caprock and the underlying brine. Considering the typically strong density difference between CO_2 and brine, as well as the large length-to-height aspect ratio of a

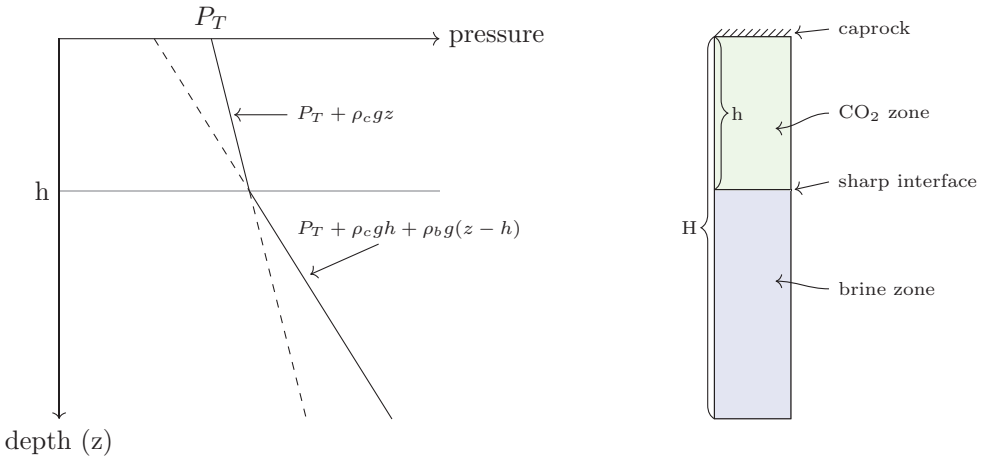

Fig. 2. Reconstructed pressure and saturation profiles from h and P_T, under the sharp-interface vertical equilibrium assumption. *Left:* Hydrostatic pressure profile. Extrapolated phase pressures shown as dashed lines. *Right:* Saturation profile along a vertical column with plume thickness h and aquifer thickness H.

typical aquifer, these assumptions are frequently reasonable [15,25]. These assumptions allow for reconstruction of vertical pressure and saturation profiles from a dimensionally reduced set of upscaled variables. For the purpose of presentational clarity, we limit ourselves to the case with vertically constant porosity and permeability, no residual saturation and a sharp interface between phase regions, although neither of these assumptions are strictly required. As upscaled variables, we use fluid pressure at the caprock level P_T and local CO_2 plume thickness h, both of which are functions of lateral coordinates only. With the simplifications above, the 3D reconstruction of pressure and saturation becomes (see also Figure 2):

$$s_c(x,y,z) = \begin{cases} 1\ ,\ z < h(x,y) \\ 0\ ,\ z > h(x,y) \end{cases} \tag{11}$$

$$p(x,y,z) = \begin{cases} P_T(x,y) + \rho_c g z & ,\ z \le h(x,y) \\ P_T(x,y) + \rho_c g h + \rho_b g(z-h) & ,\ z > h(x,y) \end{cases} \tag{12}$$

Above, s_c represents CO_2 saturation, g the gravitational constant and ρ_c and ρ_b the CO_2 and brine densities, respectively. p represents local fluid pressure (individual phase pressures are indicated by dashed lines on Figure 2, but not strictly needed here as our particularly simple saturation profile has only one phase present at any given point).

The upscaled equations are obtained by vertical integration of (8) from top to bottom of the aquifer. The reader is referred to previously published literature, e.g. [12,26], for details on the integration process. Here we limit ourselves to presenting the resulting equations, which for CO_2 are:

$$\phi \frac{\partial h}{\partial t} + h\left[\left(\frac{\phi}{K_{f,c}} + \frac{1}{K}(1-\alpha)(\alpha-\phi)\right)\frac{\partial P_T}{\partial t} + \alpha\frac{\partial \bar{\epsilon}}{\partial t}\right] + \nabla_\parallel \cdot \mathbf{Q} = \Psi_c \tag{13}$$

$$\mathbf{Q} = -\Lambda_c K_\parallel \left(\nabla_\parallel P_T - \rho_c g \nabla_\parallel \zeta\right) \tag{14}$$

Newly introduced symbols here include $\bar{\epsilon}$ (vertically averaged volumetric strain), $\mathbf{Q}$ (upscaled Darcy flux), Φ (upscaled CO_2 source term), $\Lambda_c = h/\mu_c$ (upscaled mobility) and ζ which represents caprock depth as a function of lateral coordinates. In addition, the symbol $\nabla_\parallel$ represent the two-dimensional del operator. The upscaled equations for brine are similar, as long as h is substituted by $H - h$ (H being the local thickness of the aquifer), subscript c by subscript b, and subtracting the additional term $(\rho_b - \rho_c)g\nabla_\parallel h$ from the expression inside parentheses of (14).

3. Decoupling the model

3.1. Geertsma's uniaxial poroelastic expansion coefficient

For standard reservoir simulation, the impact of changes in pore volume due to pressure-induced rock deformation is usually approximated using a pore volume compressibility coefficient c_ϕ, which amounts to substituting the rock-related part of the expression within brackets in (8), i.e. $\frac{1}{K}(1-\alpha)(\alpha-\phi)\frac{\partial p}{\partial t} + \alpha\frac{\partial \epsilon}{\partial t}$ with simply $c_\phi \frac{\partial p}{\partial t}$. For this, the strain-dependent term must be reformulated as $\alpha\frac{\partial \epsilon}{\partial p}\frac{\partial p}{\partial t}$, and some constant must be chosen to approximate the factor $\frac{\partial \epsilon}{\partial p}$. An exact representation is not possible, since volumetric strain at a given point x theoretically depends on the aquifer-wide pressure field, not only the pressure at x. However, a reasonable approximation can be obtained from the chosen poroelastic parameters by assuming zero lateral strain and constant vertical (total) stress. In that case, we have:

$$\frac{\partial \epsilon}{\partial p} = \frac{\alpha}{K_v} = c_m \tag{15}$$

where K_v is the rock's *uniaxial bulk modulus*, which is related to the bulk K and shear G moduli as $K_v = K + 4/3G$. The constant c_m, defined by (15), is called *Geertsma's uniaxial poroelastic expansion coefficient* [24]. The assumptions of zero lateral strain and constant vertical stress describe the situation of an uniform pressure increase in an horizontal, flat and infinite aquifer embedded in a larger rock matrix with a free-moving top surface at constant load. By symmetry, any deformation (and thereby strain) will be vertical in this case.

Incidentally, it can be shown that c_m also exactly describes the relation between local pressure and volumetric strain in a unbounded, homogeneous 3D domain [24], for *any* pressure field (i.e. not necessarily uniform). This suggests that in the general case, any non-local influence of pressure on volumetric strain must in some way be related to boundary conditions or inhomogeneities in the poroelastic properties of the medium.

3.2. Numerical generalization of Geertsma's coefficient

The use of Geertsma's poroelastic expansion coefficient to determine a good value for c_ϕ can be generalized in order to take general boundary conditions and elastic heterogeneities into account. To do this, we consider the interpretation of c_m as the volumetric expansion resulting from a uniform pressure increase in an infinite flat aquifer. For a specific simulation model with arbitrary boundary conditions, irregular geometry and heterogeneities, we define an spatially dependent parameter that represent the volumetric change caused by a uniform pressure increase throughout the flow domain. This parameter, which will equal c_m for the infinite, uniform case, can be numerically obtained by using a mechanics solver. In general, the obtained volumetric strain field c_m^{num} will not be uniform due to the influence of boundary conditions, nonuniform geometry or heterogeneous elastic properties. For instance, regions close to a clamped (zero displacement) boundary will generally have lower values for c_m^{num}. As a consequence, each cell in the simulation grid will be attributed its own specific value of c_ϕ. A 2D example is presented in Figure 3, where we have used a finite-element based solver to compute the volumetric strain in a horizontal aquifer embedded in a larger rock matrix, induced by a uniform pressure increase. On the figure, we plot $\Delta\epsilon/\Delta p$ computed under two different sets of lateral boundary conditions, "clamped" or "roller", and compare with the theoretical value of c_m. ("Roller" conditions here refer to zero lateral displacement and fixed vertical stress, whereas "clamped" conditions refers to zero displacement in all directions). As can be seen from the illustration, roller boundary conditions leads to a uniform c_m^{num} field that is practically coincident with c_m, whereas clamped conditions lead to a field that is similar to c_m away from boundaries and considerably attenuated towards the edges. Parameters used to generate this example are provided in Table 1. In Section 4, we compare the approach of using c_m^{num} with the more sophisticated method described in 3.3, as well as the solution from a fully coupled model.

3.3. The use of precomputed response functions

By using Geertsma's expansion coefficient (or its numerical generalization) to model pore volume changes, we presuppose that volumetric strain in the aquifer depends solely on local pressure. However, the volumetric strain at any point theoretically depends on the *global* pressure field obtained by solving the full poroelastic equations.

Table 1. Parameter values used for example presented in 3.2

Parameter	Value
Dimensions	2 (x, z)
Aquifer length/thickness	10 km / 100 m
Overburden thickness	950 m
Biot-Willis coefficient (α)	0.9
Aquifer bulk and shear moduli	10 GPa / 0.8 GPa
Surrounding rock bulk and shear moduli	40 GPa / 10 GPa

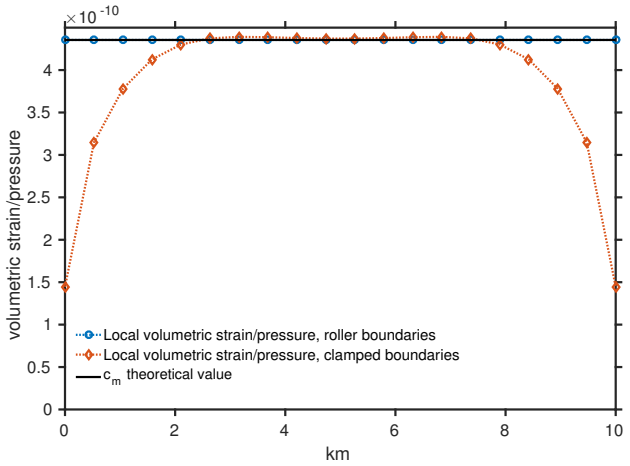

Fig. 3. Computing c_m^{num} for a two-dimensional flat and horizontal aquifer. The x-axis represents spatial position along the aquifer, whereas the y-axis represents the local change in volumetric strain for a unit, global pressure increase throughout the aquifer domain.

Reciprocally, a localized pressure perturbation will lead to global changes in volumetric strain. As long as boundary conditions do not change, changes in volumetric strain will only depend on changes in the pressure field, which means that any given pressure field is associated with a unique volumetric strain field. Since our equation system is linear, the impact on global volumetric strain from changes to the global pressure field can be obtained using the principle of superposition. If we for each function in our pressure basis precompute the associated impact on the global volumetric strain field, we can later reconstruct the exact volumetric strain associated with *any* pressure field by summing up the contributions. More formally, if we consider our pressure basis to consist of the m functions $\{\phi_i\}_{i=1\ldots m}$, the pressure field is expressed using scalar coefficients $\{p_i\}_{i=1\ldots m}$ as:

$$p(x) = \sum_{i=1}^{m} p_i \phi_i(x) \tag{16}$$

We note the *initial* pressure field p^0 with coefficients $\{p_i^0\}_{i=1\ldots m}$, and define $\tilde{p} = p - p^0$ and $\tilde{p}_i = p_i - p_i^0$, pressure can also be expressed as:

$$p(x) = p^0 + \tilde{p} = p^0 + \sum_{i=1}^{m} \tilde{p}_i \phi_i \tag{17}$$

The volumetric strain field ϵ depends linearly on pressure p, boundary conditions **bc** and body forces **f**, and can be formally divided in two parts:

$$\begin{aligned} \epsilon &= \epsilon(p, \mathbf{bc}, \mathbf{f}) \\ &= \epsilon(p^0, \mathbf{bc}, \mathbf{f}) + \epsilon(p - p^0, 0, 0) \\ &= \epsilon^0 + \tilde{\epsilon}(\tilde{p}) \end{aligned}$$

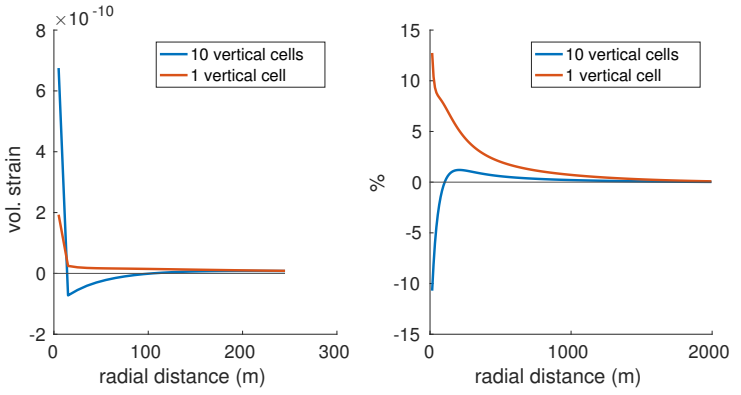

Fig. 4. Example of a response function. The curves represent volumetric strain as a function of distance from a central pressure perturbation. The left plot includes the value of the perturbed gridcell itself. On the right plot, the central value is suppressed and the curves rescaled to show percent-wise magnitude compared with the (removed) central value. The vertical grid resolution of the aquifer is 10 cells for the blue curves, and a single cell for the red curves. With just one vertical cell, the internal bulging effect in the aquifer is not captured, which significantly changes the nature of the response.

We here use ϵ^0 to denote initial volumetric strain, and $\tilde{\epsilon}$ to denote the change in ϵ caused by $\tilde{p}$, considering boundary conditions and body forces fixed. We further have:

$$\tilde{\epsilon}(\tilde{p}) = \tilde{\epsilon}\left(\sum_{i=1}^{m} \tilde{p}_i \phi_i\right) = \sum_{i=1}^{m} \tilde{p}_i \tilde{\epsilon}(\phi_i) \tag{18}$$

Knowing the set of response functions $\{\tilde{\epsilon}(\phi_i)\}_{i=1\ldots m}$ will therefore allow us to determine the volumetric strain field associated with any pressure field that can be expressed in the basis $\{\phi_i\}_{i=1\ldots m}$. We also have:

$$\frac{\partial \epsilon}{\partial p_i} = \frac{\partial \tilde{\epsilon}}{\partial p_i} = \tilde{\epsilon}(\phi_i) \tag{19}$$

By replacing the use of c_m in 3.1 with $\epsilon(\phi_i)$, we establish a set of *non-local* pore volume compressibility coefficients c_ϕ to use with the flow equation. These will exactly represent the impact of mechanics on flow, thereby eliminating the need for coupling with the mechanical system when running the simulation. The response functions $\{\tilde{\epsilon}(\phi_i)\}_{i=1\ldots m}$ can be computed at grid generation time and stored along with the grid description. Although volumetric strain is defined on Ω, we only need to keep track of the part covering Ω_A. Assuming that the response functions are made available as part of the input data, the only substantial change necessary for a standard flow simulator to model geomechanical impact is added support for non-local pore volume compressibility coefficients. However, the applicability of the method hinges on a few practical observations/points, which we now proceed to address.

Table 2. Parameter values used to compute the response illustrated in Figure 4

Parameter	Value
Aquifer thickness / depth	100 m / 1000 m
Aquifer/overburden Young's modulus	1 GPa / 10 GPa
Perturbation radius	10 m (1 cell)
Perturbation height	100 m (height of aquifer)
Impulse magnitude	1 Pa
Grid block size	10 m
Vertical aquifer resolution	1 cell (red), 10 cells (blue)

First, although theoretically the support of each $\tilde{\epsilon}(\phi_i)$ is global, the response tends to decay quickly as the distance from the support of ϕ_i grows. This behavior can to some degree be attributed to the free-moving top surface (not of the aquifer itself but of the full mechanical domain including the overburden). On Figure 4 we see the radial profile

of a response function computed for a cylindrical pressure perturbation in a horizontal aquifer (parameters given in Table 2). By examining the blue curve, we see that the change in volumetric strain is by far largest within the support of the perturbation itself. It then drops to a negative value in the immediate neighborhood, reflecting compression caused by the expanding center region, and then rises to a positive value associated with the effect of caprock uplift, after which it gradually decays to zero. If the horizontal resolution of the mechanical grid inside the aquifer is too low, the compression caused by the expanding central region on its neighborhood is not properly captured, and the response function changes both quantitatively and qualitatively (red curves on Figure 4).

The relatively localized impact of the response functions means that they do not need to be stored in their entirety. As the magnitude of $\tilde{\epsilon}(\phi_i)$ drops below a specified small threshold value, it can be truncated with little loss of precision in the final simulation result. Truncation means that the matrix of stored responses can be stored in a sparse format, which may be crucial for grids with a large number of cells. A sparse matrix structure is also a practical necessity when solving large linear systems using iterative approaches.

When a response function is truncated, it also needs to be rescaled to ensure that the total volumetric change in the aquifer is preserved. Interestingly, if ϕ_i is defined as the indicator function on gridcell i (i.e. equal to one inside cell i and zero elsewhere), it can be shown [23] that we have the following (exact) relation:

$$\int_{\Omega_A} \tilde{\epsilon}(\phi_i)\mathrm{dx} = (c_m^{\mathrm{num}})_i \tag{20}$$

where $(c_m^{\mathrm{num}})_i$ here denotes the value of c_m^{num} on cell i. This signifies that the approach based on precomputed response functions and cell indicator functions as pressure basis has the following two limit cases: (1) it reproduces the fully coupled model when the truncation threshold goes to zero; (2) it becomes equivalent with the local approach described in 3.2 when the truncation threshold is raised high enough to concentrate the whole response within a single gridcell.

For the computation of volumetric strain responses, other choices of pressure basis functions are of course possible. For instance, a coarser basis where ϕ_i represents a whole vertical pillar of cells in the aquifer is a natural choice when the flow equations are formulated under the VE assumption, since the vertical pressure profile will then have to be reconstructed anyway. Since the key assumption behind VE models is hydrostatic pressure, a given overpressure at the top of the aquifer will translate to a similar overpressure throughout the vertical column. The use of pressure basis functions representing vertical stacks of cells becomes natural, and significantly reduces the number of responses that must be precomputed. There is a slight approximation involved in this approach, since there is a kink in the hydrostatic pressure profile in the presence of CO_2 (c.f. Figure 2). However, by using the phase-weighted pressure average specified in (10) to compute the average pressure perturbation in a column, the introduced error remains small.

The initial computation of response functions is expensive, since each basis function (in principle) requires a separate solution of the linear elasticity equations. However, the complete task needs to be carried out only one time, as part of the grid generation process. Moreover, there are some ways to make the computation more efficient. Since the magnitude of the response functions can be practically neglected beyond a certain distance, it is possible to compute several responses in a single solve, as long as they remain sufficiently spatially separated. In addition, since only the right-hand side of the equation system changes for each solution, it is beneficial to invest some initial time in computing a good preconditioner for the system. Finally, the task is trivially parallelizable across multiple processing cores, since each response function can be computed completely independently of the others.

4. Results

In this section, we compare the different approaches of modeling geomechanical impact on flow with a two-phase VE model applied on a couple of CO_2 injection examples. Our first example is a 2D model where CO_2 is injected with a fixed bottom-hole pressure into a thin, closed reservoir of limited extent. The second example is a 3D case where we consider a fixed-rate CO_2 injection into an open formation.

For both examples we aim to enhance the non-local interdependence between pressure and volumetric strain by specifying a relatively strong contrast in elastic properties between aquifer and surrounding rock. To introduce local variations in the pressure field, We moreover define a heterogeneous and strain-dependent permeability field, where initial permeability of the rock, k_0 is set to a realization of a quasi-gaussian scalar field with a specified average value. Permeability k is dynamically linked to the current porosity value ϕ (resulting from changes in pressure and volumetric

strain) through the relation [27]:

$$k = k_0(\phi/\phi_0)^{\alpha} \tag{21}$$

We here use an exponent value of $\alpha = 20$, which is in the upper range of values experimentally reported in [27], and which for the pressure differentials in our examples never lead to local permeability changes significantly exceeding a factor of two.

The density and compressibility of CO_2 are computed from local conditions using an equation of state [28], whereas the significantly less compressible water is modeled using a linear relation.

We compare the solutions obtained from the precomputed response and from the approaches using (local) pore volume compressibility coefficients with the solution of the fully coupled system, used as reference. For both examples, pressure responses were truncated at 1×10^{-3} of their central value. The fully coupled solution was computed using an iterative scheme based on operator splitting. For the second example, we also compare computational runtimes.

The numerical code was developed in-house using MATLAB, based on functionality from the Matlab Reservoir Simulation Toolbox (MRST) [29] and its CO_2 storage module `MRST-co2lab` [30]. A fully-implicit, first order, finite-volume discretization scheme was used for the VE flow equations, whereas the mechanics equations were discretized using virtual elements [31] supplied with additional stiffness terms for correct modeling of higher-order energies, effectively making the scheme equivalent with a first-order finite-element approach as long as cell shapes are restricted to prisms.

4.1. 2D example: fixed-pressure injection into a closed formation

In this first example, we consider a thin (10 m), closed reservoir Ω_A consisting of soft rock at a depth of 1000 m, embedded in a considerably stiffer surrounding rock matrix Ω_S. Distance measurements are given in Figure 5, whereas other simulation parameters are listed in Table 3. A vertical average of the stochastically generated permeability field in the reservoir is shown in Figure 6. During the total simulated period of 1000 days, CO_2 is continuously injected at a fixed bottom-hole pressure into the middle of the reservoir (x = 2 km). We compare the resulting pressure field and CO_2 plume thickness obtained from using: (1) fully coupled geomechanics ("full"); (2) precomputed responses ("pr"); (3) local poroelastic expansion coefficients based on numerically computed c_m^{num} ("local"); and (4) local poroelastic expansion coefficients based on Geertsma's uniaxial expansion coefficient c_m ("uniform").

The "pr" model uses precomputed responses for each of the 161 vertical columns in the reservoir. In order to illustrate their shape and extent, five of these are drawn in the left plot of Figure 7, where their relatively local extent can be clearly seen. Away from the boundary, the responses have a very similar shape, which is to be expected given the simple geometry and the constant elastic parameters in each of Ω_S and Ω_A. Compared with Figure 4, the responses drawn here do not exhibit a local compression region. This is explained by the very thin nature of the reservoir compared to the lateral extent of each pillar, which constitutes the support of each pressure basis function. As a consequence, any local bulge effect is overwhelmed by the caprock uplift effect. In the right plot in the same figure, we see the values for c_m^{num} and c_m, used in the "local" and "uniform" models respectively.

Reservoir pressure and CO_2 plume thicknesses corresponding to day 1, day 10 and day 100 are shown in Figure 8. At day 10, there is a noticeable discrepancy in pressure between the "full" and "pr" models on one hand, and the "local" and "constant" models on the other. At day 100, pressures from all models are roughly in agreement, whereas at day 1000, the "constant" model diverges from the other. This is to be expected since at this point the induced pressure increase has reached the lateral boundaries, and the use of c_m in the "constant" model does not capture any information regarding specific boundary behavior. Regardless of pressure differences, the impact on the CO_2 plume appears to be very small, with all models in good agreement for all selected timesteps.

4.2. 3D example: fixed-rate injection into open aquifer

In our second example, we apply our models to a 3D model where CO_2 is injected at a constant rate into an open aquifer of constant thickness (20 m) at a depth of 1800 m. The simulation model can thus be considered to consist of three layers: the overburden (extending from surface level down to aquifer), the aquifer itself, and the underburden (extending from the aquifer bottom downwards to a depth of 4000 m). Contrary to the first example, the flow domain here extends out to the lateral boundaries of the model, where a fixed, hydrostatic, pressure boundary condition is

Table 3. Parameter values used in the 2D example of subsection 4.1

Parameter	Value
Reservoir thickness (m)	10
Lateral resolution (cells)	201
Vertical resolution (cells)	10 (Ω_S above Ω_A) / 4 (Ω_A) / 10 (Ω_S below Ω_A)
Young's modulus (GPa)	20 (in Ω_S) / 1 (in Ω_A)
Poisson's ratio	0.3 (in $\Omega_S \cup \Omega_A$)
Biot-Willis coefficient	1
Reservoir porosity	0.2
Average permeability (millidarcy)	8.8
Brine density (kg/m^3)	1000
Brine bulk modulus (GPa)	2.5
Viscosity (Pa·s)	8.0×10^{-4} (brine) / 6.0×10^{-5} (CO_2)
Initial (hydrostatic) pressure at caprock (MPa)	10
Reservoir temperature (°C)	40
Injection overpressure (MPa)	10
pressure response truncation value	1.0×10^{-3}
Solution computed for the following days	1, 10, 20, 50, 100, 150, 200, 400, 800, 1000

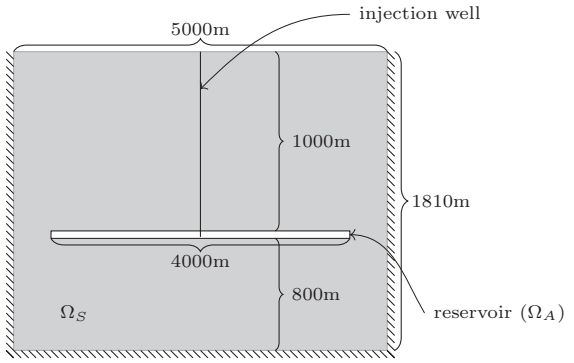

Fig. 5. Diagram of simulation domain used in example of subsection 4.1. The long, white rectangle in the middle represents the reservoir, whereas the gray area represent the surrounding rock matrix. Mechanical boundary conditions are set to zero-displacement at the bottom and the sides, and constant stress (atmospheric pressure) on top.

imposed. For the mechanics, clamped conditions are used at the bottom, roller conditions at the sides, and constant stress (atmospheric pressure) on top. Other relevant simulation parameters are provided in Table 4. Given the uniform geometry, the roller boundary conditions and the constant elastic parameters within Ω_A and Ω_S, there is no difference between c_m and c_m^{num}, so we do not make a distinction, but simply refer to the "local" model. A vertical average of the stochastically generated aquifer permeability field used is shown in Figure 9.

Simulation results are shown in figures 10–13. On Figure 10, we show a top view of the aquifer pressure field for the first day after injection start as well as after two years of continuous injection. We also plot the error introduced by our two approximate methods ("pr" and "local"). We see that for both timesteps, the error from the "pr" model remains at the order of 1×10^{-3} or less, whereas the "local" model initially has a maximal error of about 8 percent, which is reduced to an error comparable with the "pr" model after two years. For both approximate models, but in particular for the "local" model, the errors are mainly concentrated in a small area around the injection well, where pressure variation is largest. On Figure 11 we show a similar analysis for CO_2 plume height. The solution for the full model shows a somewhat irregular, star-shaped plume extending out to the lateral boundaries. The irregular shape is caused by the heterogeneous permeability field. The errors introduced by the "pr" and "local" models remain very small at all times. Interestingly, the error becomes zero around the injection well after two years, which is to be expected since the plume then extends all the way down to the aquifer bottom. On Figure 12 and Figure 13, we plot cross-sections of pressure and CO_2 plume profiles along with the errors introduced by the "pr" and "local" models.

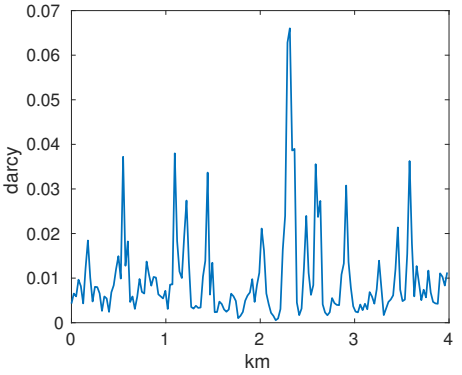

Fig. 6. Reservoir permeability field used for example in subsection 4.1. Mean value is 0.01 darcy.

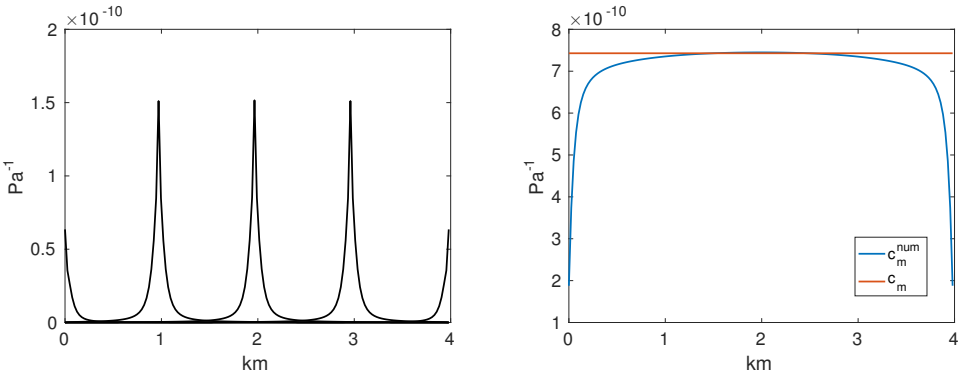

Fig. 7. *Left:* response functions corresponding to unit pressure impulses at five selected reservoir columns (example in subsection 4.1). *Right:* Cell-wise values of c_m, used to compute compressibility coefficients for the "constant" model; and c_m^{num}, used to compute compressibility coefficients for the "local" model (example in subsection 4.1).

We see that while the "pr" model performs better than the "local" model, the only significant errors are found in the pressure field, and only around the injection area at the beginning of the simulated period.

Finally, we have a look at the associated computational requirements. Table 5 presents the time spent on computing the simulation, using the three different models. Care should be taken when interpreting these numbers, considering the prototype nature of the simulation software used. The figures nevertheless suggest that the precomputed responses approach may provide a considerable computational advantage compared to the fully coupled model, but still introduces compared to the "local" model. The reason the "pr" model requires more computation than the "local" model despite not introducing additional equations or unknowns is the less sparse nature of the linear equations involved, which requires additional time for the iterative linear solvers ("bicgstab", in this case) to handle. Also, the initial computation of response functions took 3500 seconds. This, however, is a cost that incurs only once.

5. Discussion

In this paper we have explained and tested a few approaches for including the effects of geomechanics on two-phase flow. We did this in the setting of modeling CO_2 injection using a vertical equilibrium framework. The approximate approaches do not require coupling with a mechanics solver at runtime, thus simplifying the workflow and freeing up computational resources.

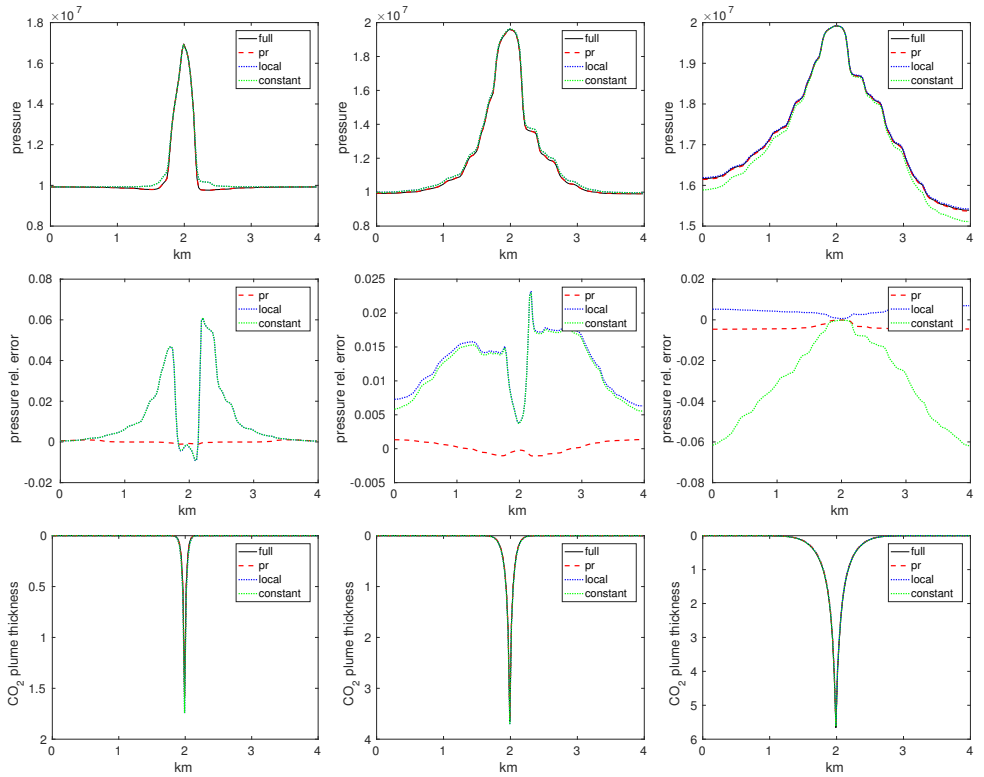

Fig. 8. Selected timesteps of simulation results from example in subsection 4.1. Columns represent day 10 (left), day 100 (middle) and day 1000 (right). The upper row shows the pressure field at the top of the reservoir, using the four different methods. The middle row shows the *relative* error between each of the three approximate approaches ("pr", "local" and "constant") compared to the benchmark ("full"). The relative error is obtained by dividing pressure discrepancy by total pressure variation. The bottom field shows CO_2 plume thicknesses (y-axis inverted to illustrate actual plume shape).

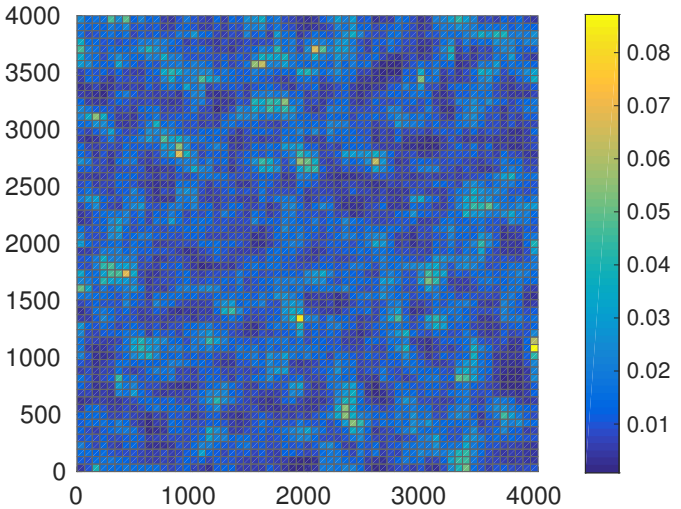

Fig. 9. Aquifer permeability field used for the example in subsection 4.2 (units in darcy). Mean value is 13 millidarcy.

Table 4. Parameter values used in the 3D example of subsection 4.2

Parameter	Value
Lateral extent (km)	4 (east-west and north-south)
Aquifer depth (m)	1800
Aquifer thickness (m)	20
Lateral resolution (cells)	61
Vertical resolution (cells)	10 (Ω_S above Ω_A) / 4 (Ω_A) / 10 (Ω_S below Ω_A)
Young's modulus (GPa)	20 (in Ω_S) / 6 (in Ω_A)
Poisson's ratio	0.15 (in Ω_S) / 0.2 (in Ω_A)
Biot-Willis coefficient	0.9
Reservoir porosity	0.17
Average permeability (millidarcy)	13
Initial (hydrostatic) pressure at caprock (MPa)	17.8
Reservoir temperature (°C)	90
Brine density (kg/m^3)	1000
Brine bulk modulus (GPa)	2.5
Viscosity (Pa·s)	3.2×10^{-4} (brine) / 6.0×10^{-5} (CO_2)
Injection rate (m^3/s)	0.02
pressure response truncation value	1.0×10^{-3}
Solution computed for the following days	1, 5, 10, 30, 365, 730

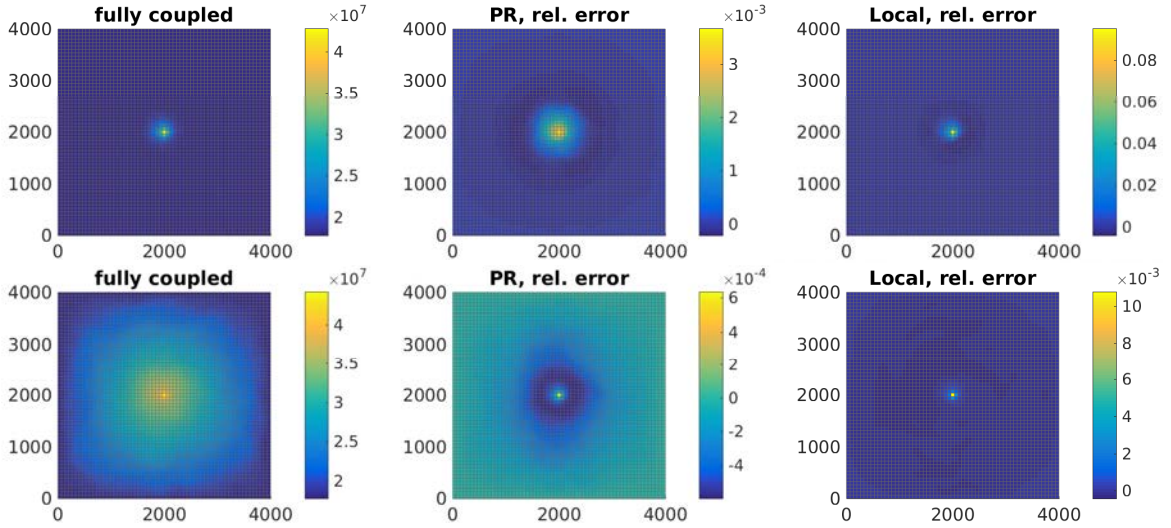

Fig. 10. Top view of aquifer pressure field (in Pa) at caprock level, after 1 day (top row) and after two years (bottom row) of CO_2 injection. The left column represents the "benchmark" result obtained by the fully coupled model. The middle and right columns represent the relative errors of the "pr" and the "local" models, respectively (ratio of pressure discrepancy to total pressure variation).

Table 5. Computing time for the different approaches

Approach	Runtime (seconds)
Fully coupled (splitting scheme)	1262
Precomputed responses	81.8
Local, using c_m^{num}	6.4

It should be pointed out that none of the approaches for modeling geomechanics *require* flow equations to be based on the VE assumption. In particular, the model using precomputed responses can equally well be applied in the setting of a full 3D reservoir simulator, and in fact, our results indicate that situations requiring full 3D simulations may be the most relevant use cases for the precomputed response approach. This is because, at least for the cases presented in

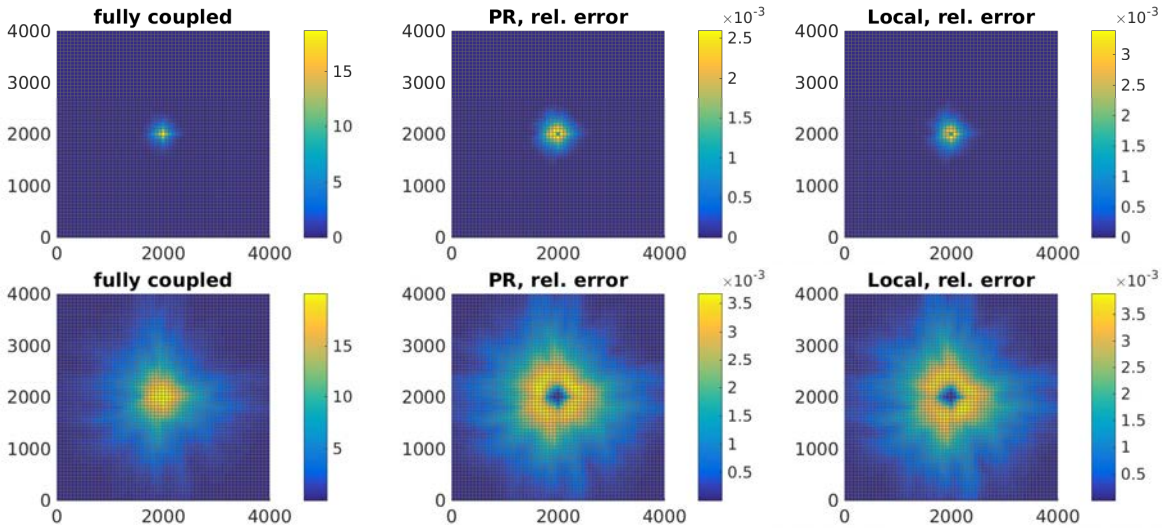

Fig. 11. Top view of CO_2 plume thickness (in meters), after 1 day (top row) and after two years (bottom row) of CO_2 injection. The left column represents the "benchmark" result obtained by the fully coupled model. The middle and right columns represent the relative errors of the "pr" and the "local" models, respectively (local height discrepancy divided by maximum plume height) .

this paper, the local model based on c_m^{num} appears to produce good results except for at early times around the injection well. However, the use of VE models is most relevant at larger spatial and temporal scales. A simple estimate of the time T_{dr} necessary for brine to drain out of a CO_2 plume, resulting in fluid segregation, was presented in [32] as:

$$T_{\text{dr}} \sim \frac{H\phi}{\lambda_{\text{br}}^* k \Delta\rho g} \tag{22}$$

with H being aquifer thickness, ϕ porosity, k permeability, $\Delta\rho$ density difference between brine and CO_2 and g the gravitational constant. In addition, λ_{br}^* represents a characteristic brine mobility. If we apply this formula on the two examples examined in the previous section and assume $\lambda_{\text{br}}^* = \frac{1}{2\mu_b}$ (with μ_b being brine viscosity), we obtain values T_{dr} that are just short of 2 years in both cases. However, by this time the impact of geomechanical deformation appears to be equally well represented using the local model based on c_m^{num}. There may be other cases where the geomechanical impact of CO_2 injection and migration requires a more sophisticated model for mechanics at temporal scales relevant for VE simulation, but so far most of our experiments involving realistic parameters indicate that the use of c_m^{num} remains a good approximation. Even if variations in caprock geometry are introduced, leading CO_2 to collect in structural traps, the additional capillary overpressure (difference between broken and whole line at caprock level in Figure 2) is generally not large or abrupt enough to introduce a significant difference between the "local" and the "pr" model above.

Another point to mention is that the discretization of the mechanical grid does matter. If the discretization is too coarse, the resulting error in volumetric strain may be more important than the improvement we seek to obtain by coupling geomechanics with the flow model in the first place. One example is provided by the red graph in Figure 4, which demonstrates the importance of vertical resolution within the aquifer. Another example is shown in Figure 14, where we for a 2D test example plot the global volumetric strain profile induced by a 476 meters wide, unit pressure increase in a 50 meter thick, horizontal aquifer, using different lateral grid resolutions. The coarsest grid, where the pressure increase is exactly covered by one grid cell, leads to a volumetric strain profile that is significantly more spatially spread out compared to solutions obtained using progressively finer grids. The volumetric strain profile appears to converge to something that is in-between the coarse solution and the approximated strain obtained from simply multiplying the pressure perturbation by c_m (indicated by black dots). This indicates that a sufficiently high grid resolution is needed in order for the full coupling of a geomechanics model to provide any real improvement in precision compared to the simple use of a local multiplier in the flow model.

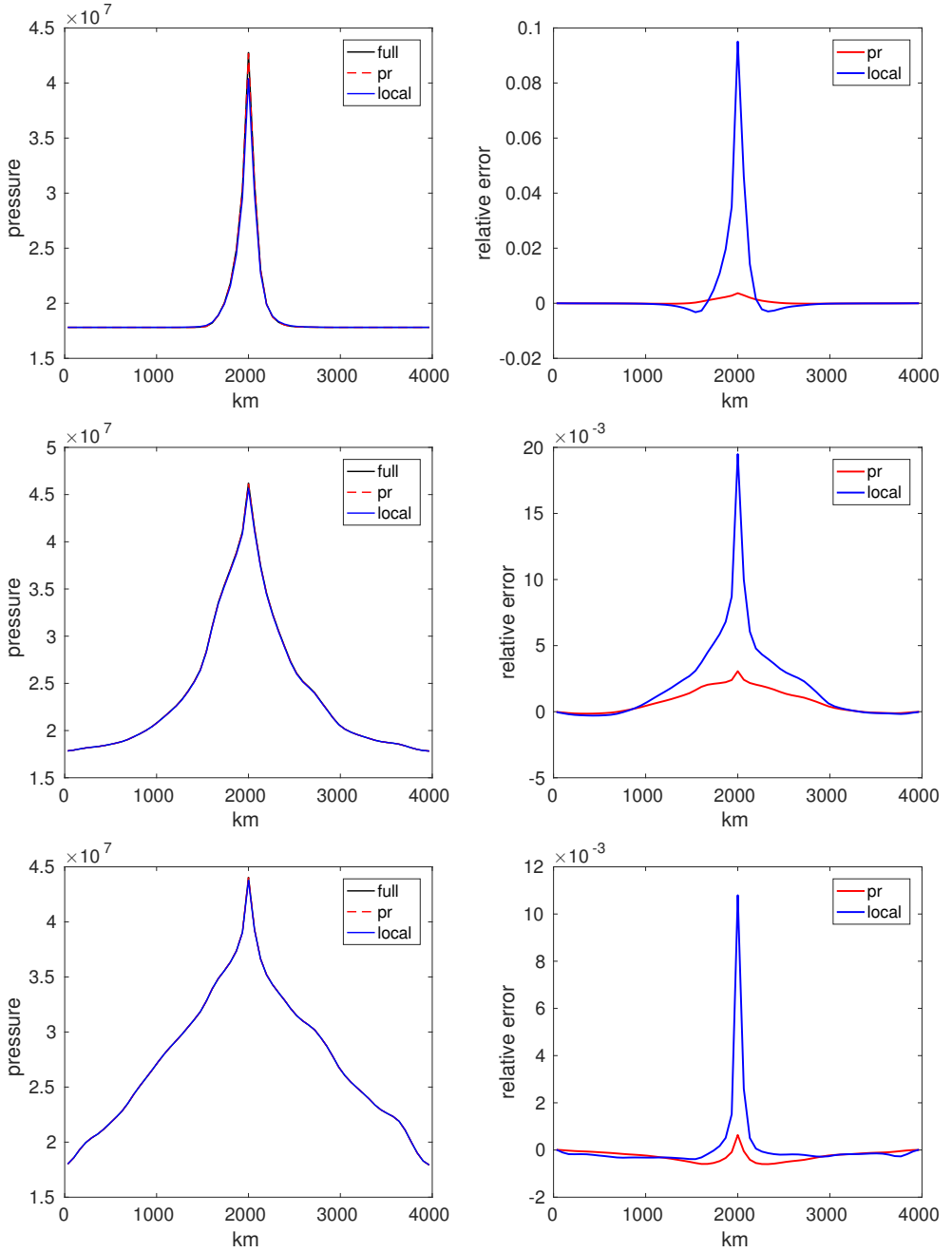

Fig. 12. Cross-section plot of pressure field at top of aquifer (left column) and model relative error (right column) for the simulation in subsection 4.2. Results are plotted for the aquifer state after 1 day (top row), 1 month (middle row) and two years (bottom row). Relative error is defined as model discrepancy divided by total pressure variation.

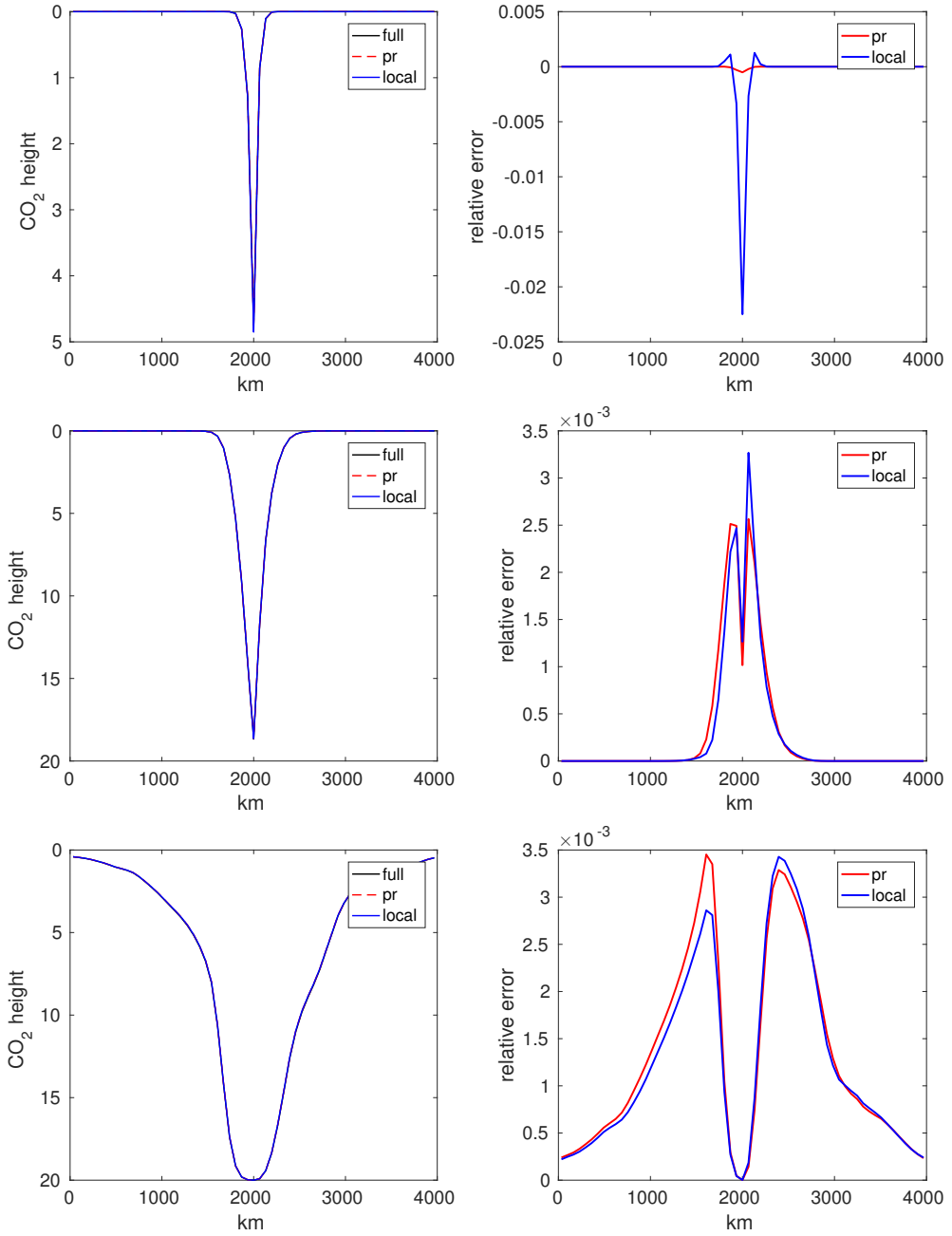

Fig. 13. Cross-section plot of CO_2 plume (left column) and model relative error (right column) for the simulation in subsection 4.2. Results are plotted for the aquifer state after 1 day (top row), 1 month (middle row) and two years (bottom row). Relative error is defined as model discrepancy divided by maximal plume height.

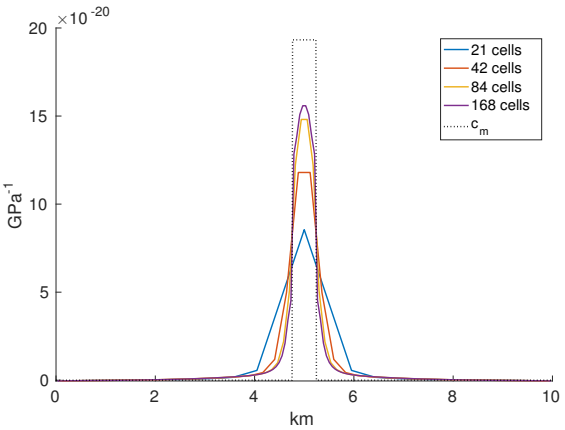

Fig. 14. Volumetric response (2D case) for a unit, 476 meter wide pressure perturbation, computed using progressively finer lateral grid resolutions.

We therefore foresee that in most situations, the use of pore volume compressibility coefficients derived from c_m^{num} is likely to provide the best trade-off between precision and computational resources when using VE models to investigate long-term, large-scale CO_2 storage issues. For simulation of shorter periods, where full 3D equations is the more natural choice, the use of precomputed responses to model the full impact of geomechanics can be a more attractive option.

Acknowledgments

This work was funded by the MatMoRa-II project, Contract no. 21564, sponsored by the Research Council of Norway and Statoil ASA.

References

[1] Energy technology perspectives 2016 - executive summary, International Energy Agency (IEA) (2016).
[2] J. Rutqvist, C.-F. Tsang, A study of caprock hydromechanical changes associated with CO_2-injection into a brine formation, Environmental Geology 42 (2) (2002) 296–305. doi:10.1007/s00254-001-0499-2.
[3] M. Y. Darcis, Coupling models of different complexity for the simulation of CO_2 storage indeep saline aquifers.
[4] M. Preisig, J. H. Prévost, Coupled multi-phase thermo-poromechanical effects. case study: CO_2 injection at In Salah, Algeria, International Journal of Greenhouse Gas Control 5 (4) (2011) 1055–1064.
[5] J. Kim, Sequential methods for coupled geomechanics and multiphase flow, Ph.D. thesis, Stanford University (2010).
[6] A. Mikelić, M. F. Wheeler, Convergence of iterative coupling for coupled flow and geomechanics, Computational Geosciences 17 (3) (2013) 455–461.
[7] I. S. Ligaarden, H. M. Nilsen, Numerical aspects of using vertical equilibrium models for simulating CO_2 sequestration, in: Proceedings of ECMOR XII–12th European Conference on the Mathematics of Oil Recovery, EAGE, Oxford, UK, 2010.
[8] H. M. Nilsen, P. A. Herrera, M. Ashraf, I. Ligaarden, M. Iding, C. Hermanrud, K.-A. Lie, J. M. Nordbotten, H. K. Dahle, E. Keilegavlen, Field-case simulation of CO_2-plume migration using vertical-equilibrium models, Energy Procedia 4 (0) (2011) 3801–3808. doi:10.1016/j.egypro.2011.02.315.
[9] J. C. Martin, Some mathematical aspects of two phase flow with application to flooding and gravity segregation, Prod. Monthly 22 (6) (1958) 22–35.
[10] K. H. Coats, R. L. Nielsen, M. H. Terune, A. G.Weber, Simulation of three-dimensional, two-phase flow in oil and gas reservoirs, Soc. Pet. Eng. J. Dec (1967) 377–388.
[11] J. C. Martin, Partial integration of equation of multiphase flow, Soc. Pet. Eng. J. Dec (1968) 370–380.
[12] J. M. Nordbotten, M. A. Celia, Geological Storage of CO_2: Modeling Approaches for Large-Scale Simulation, John Wiley & Sons, Hoboken, New Jersey, 2012.
[13] H. Class, A. Ebigbo, R. Helmig, H. K. Dahle, J. M. Nordbotten, M. A. Celia, P. Audigane, M. Darcis, J. Ennis-King, Y. Fan, B. Flemisch, S. E. Gasda, M. Jin, S. Krug, D. Labregere, A. N. Beni, R. J. Pawar, A. Sbai, S. G. Thomas, L. Trenty, L. Wei, A benchmark study on problems related to CO_2 storage in geologic formations, Comput. Geosci. 13 (4) (2009) 409–434. doi:10.1007/s10596-009-9146-x.

[14] J. M. Nordbotten, B. Flemisch, S. E. Gasda, H. M. Nilsen, Y. Fan, G. E. Pickup, B. Wiese, M. A. Celia, H. K. Dahle, G. T. Eigestad, K. Pruess, Uncertainties in practical simulation of CO_2 storage, Int. J. Greenh. Gas Control 9 (0) (2012) 234–242. doi:10.1016/j.ijggc.2012.03.007.
[15] J. M. Nordbotten, H. K. Dahle, Impact of the capillary fringe in vertically integrated models for CO_2 storage, Water Resources Research 47 (2). doi:10.1029/2009WR008958.
[16] S. E. Gasda, J. M. Nordbotten, M. A. Celia, Vertically averaged approaches for CO_2 migration with solubility trapping, Water Resources Research 47 (5). doi:10.1029/2010WR009075.
[17] O. Andersen, S. Gasda, H. Nilsen, Vertically averaged equations with variable density for CO_2 flow in porous media, Transp. Porous Media (2014) 1–33doi:10.1007/s11242-014-0427-z.
[18] S. E. Gasda, H. M. Nilsen, H. K. Dahle, Impact of structural heterogeneity on upscaled models for large-scale CO_2 migration and trapping in saline aquifers, Advances in Water Resourcesdoi:10.1016/j.advwatres.2013.05.003.
[19] S. Gasda, W. Gray, H. Dahle, Vertically integrated models with coupled thermal processes, European Association of Geoscientists and Engineers, EAGE, 2014.
[20] T. I. Bjørnarå, J. M. Nordbotten, J. Park, Vertically integrated models for coupled two-phase flow and geomechanics in porous media, Water Resources Research 52 (2) (2016) 1398–1417. doi:10.1002/2015WR017290.
[21] R. D. Allen, H. M. Nilsen, O. A. Andersen, K.-A. Lie, On obtaining optimal well rates and placement for CO_2 storage, in: Proceedings of ECMOR XV–15th European Conference on the Mathematics of Oil Recovery, EAGE, Amsterdam, Netherlands, 2016.
[22] H. Nilsen, S. Krogstad, . Andersen, A. Rebecca, K.-A. Lie, Using sensitivities and vertical-equilibrium models for parameter estimation of co2 injection models with application to the sleipner injection to measured data, Submitted to Energy Procedia.
[23] O. Andersen, H. M. Nilsen, S. E. Gasda, Modelling geomechanical impact of CO_2 injection using precomputed response functions, in: Proceedings of ECMOR XV–15th European Conference on the Mathematics of Oil Recovery, EAGE, Amsterdam, Netherlands, 2016.
[24] H. F. Wang, Theory of linear poroelasticity, Princeton Series in Geophysics, Princeton University Press, Princeton, NJ.
[25] Y. Yortsos, A theoretical analysis of vertical flow equilibrium, Transp. Porous Media 18 (2) (1995) 107–129. doi:10.1007/BF01064674.
[26] H. M. Nilsen, K.-A. Lie, O. Andersen, Robust simulation of sharp-interface models for fast estimation of CO_2 trapping capacity, Computational Geosciences (2015) 1–21doi:10.1007/s10596-015-9549-9.
[27] C. David, T.-F. Wong, W. Zhu, J. Zhang, Laboratory measurement of compaction-induced permeability change in porous rocks: Implications for the generation and maintenance of pore pressure excess in the crust, pure and applied geophysics 143 (1) (1994) 425–456. doi:10.1007/BF00874337.
[28] R. Span, W. Wagner, A new equation of state for carbon dioxide covering the fluid region from triple-point temperature to 1100 K at pressures up to 800 MPa, J. Phys. Chem. Ref. Data 25 (6) (1996) 1509–1597.
[29] The MATLAB Reservoir Simulation Toolbox, version 2015b, `http://www.sintef.no/MRST/` (12 2015).
[30] SINTEF ICT, The MATLAB Reservoir Simulation Toolbox: Numerical CO_2 laboratory (12 2015).
URL http://www.sintef.no/co2lab
[31] A. L. Gain, C. Talischi, G. H. Paulino, On the virtual element method for three-dimensional linear elasticity problems on arbitrary polyhedral meshes, Computer Methods in Applied Mechanics and Engineering 282 (2014) 132–160.
[32] B. Court, K. W. Bandilla, M. A. Celia, A. Janzen, M. Dobossy, J. M. Nordbotten, Applicability of vertical-equilibrium and sharp-interface assumptions in CO2 sequestration modeling, International Journal of Greenhouse Gas Control 10 (2012) 134–147. doi:10.1016/j.ijggc.2012.04.015.